Lab on a Chip

Check for updates

A planar impedance sensor for 3D spheroids†

V. F. Curto, (iD) ‡[a] M. P. Ferro,‡[a] F. Mariani, (iD) [b] E. Scavetta (iD) [b] and R. M. Owens (iD) *[ac]

Three dimensional cell culture systems have witnessed rapid expansion in the fields of tissue engineering and drug testing owing to their inherent ability to mimic native tissue microenvironments. High throughput technologies have also facilitated rapid and reproducible generation of spheroids and subsequently their use as *in vitro* tissue models in drug screening platforms. However, drug screening technologies are in need of monitoring platforms to study these 3D culture models. In this work we present a novel platform to measure the electrical impedance of 3D spheroids, through the use of a planar organic electrochemical transistor (OECT) and a novel circular-shaped microtrap. A new strategy was generated to overcome incompatibility of the integration of polydimethylsiloxane (PDMS) microdevices with OECT fabrication. The impedance platform for 3D spheroids was tested by using spheroids formed from mono-cultures of fibroblast and epithelial cells, as well as co-culture of the two cell types. We validated the platform by showing its ability to measure the spheroid resistance (R_{sph}) of the 3D spheroids and differences in R_{sph} were found to be related to the ion permeability of the spheroid. Additionally, we showed the potential use of the platform for the on-line R_{sph} monitoring when a co-culture spheroid was exposed to a porogenic agent affecting the integrity of the cell membrane.

Introduction

Recent advances in microfabrication, cell biology and tissue engineering have greatly supported the development of physiologically relevant 3D cell culture models. Through the use of these models it is now possible to create *in vitro* systems that can better mimic *in vivo* tissue dynamics with enhanced cell–cell and cell-extracellular matrix (ECM) interactions.[1,2] Generation of 3D cell models has been done using both natural and/or synthetic polymers for the fabrication of 3D porous scaffolds in which monoculture or co-cultures of cells can grow in 3D.[3] In parallel, the use of scaffold-free techniques for the formation of 3D cell constructs has also greatly advanced in recent years.[4] By taking advantage of the ability of cells to secrete their own ECM and to self-organize into stable 3D structures, cells cultured on non-adherent substrates form 3D microstructures commonly known as spheroids or organoids. Several reports have shown the development of different organoids types, such as cardiac,[5,6] liver[7,8] and epithelial[9,10] tissues, both in mono and co-culture systems.

The rapid expansion of scaffold-free technologies to create 3D spheroids, such as the hanging drop technique,[11] has opened up new opportunities in the field of drug discovery and toxicology screening. Recent efforts in this research area have made it feasible to use spheroids for high-throughput drug screening by employing well-established biology tools, such as imaging[12] and other end-point assays.[13] Microfluidics have also been explored extensively for manipulation and testing of spheroids in lab-on-a-chip devices, both for long-term culture and drug screening.[14–17] Manipulation of spheroids in microfluidics can be performed by either loading the spheroid in the microfluidic after off-chip formation, or by direct formation of the spheroid in the microchannel. For the former, semi-oval shaped nozzle microfluidic devices are typically used to trap the spheroids in microfluidics. In these systems, bypass channels of higher hydraulic resistance are used to precisely position the spheroids in the microfluidics.[14,15,18] Silva *et al.* demonstrated a reduction in the shear-fluid damage of trapped pancreatic islets when using this device geometry.[15] For spheroids formed *in situ*, different strategies have been employed such as hemispherical microwells[16] and pneumatic microstructure arrays[17] for tumor spheroid cultures, as well as the integration of microfluidic networks in hanging drop systems with a microfluidic gradient generator and capillary valves for on line toxicology studies of human colorectal carcinoma spheroids.[19]

Despite the push towards the use of spheroids for high-throughput drug discovery and toxicology, there is a definite gap in terms of available technologies capable of performing

[a] *Department of Bioelectronics, Ecole Nationale Supérieure des Mines, CMP-EMSE, MOC, 880 Avenue de Mimet, Gardanne 13541, France*
[b] *Dipartimento di Chimica Industriale 'Toso Montanari', Università di Bologna, Viale Risorgimento 4, 40136 Bologna, Italy*
[c] *Department of Chemical Engineering and Biotechnology, Philippa Fawcett Drive, CB3 0AS, Cambridge, UK. E-mail: rmo37@cam.ac.uk*
† Electronic supplementary information (ESI) available. See DOI: 10.1039/c8lc00067k
‡ These two authors contributed equally to this work.

on-line monitoring of these 3D culture models. Label-free electrochemical impedance sensors (EIS) have proven to be a very powerful technique to assess the integrity of cell barriers in a minimally invasive manner.[20] To date, EIS has been used extensively with 2D cell culture for the determination of electrical resistance of cell layers (to assess cell properties such as adhesion, proliferation or differentiation[20]) in cells grown directly on electrodes, or on porous membranes, to determine a quantity known as trans(epi/endo)-thelial resistance (TEER).[21] However, there are few examples of impedance based methods for monitoring 3D cultures.[22–24]

Our laboratory has explored the use of a novel class of organic electronic devices, the organic electrochemical transistors (OECTs), as an alternative electronic transducer to perform cell-impedance sensing.[25] The OECT has been shown to have advantages over simple electrodes due to the amplification inherent in the transistor.[25] The OECT is a three terminal device that make use of the electrochemical doping/de-doping of a conducting polymer, such as poly(3,4-ethylene-dioxythiophene):poly(styrene sulfonic acid) (PEDOT:PSS), to modulate the drain current of the transistor channel.[26] OECTs have been employed in a wide range of applications, ranging from chemo/bio-sensing,[27,28] to *in vivo* brain activity recording[29] and *in vitro* measurements of electrogenic cells[30] as well as non-electrogenic cells.[31,32] Recently, we reported on the monitoring of 3D cysts using the OECT, however the sensitivity and the ease of use of the technique left room for improvement.[33]

In this work, we show the coupling of an OECT transducer with a microfluidic trapping device to realize an easy-to-use testing platform capable of assessing the resistance of spheroids. We propose a new fabrication strategy for both the OECT and the PDMS microtrap to achieve the optimal performance of our organic impedance sensor. Through the use of a PDMS circular-shaped microtrap we validated our platform using both mono- and co-culture spheroids. The spheroids are cultured off-chip using the hanging-drop method and then easily integrated with our device, demonstrating the ability of the platform to measure the spheroid resistance for acute toxicology measurements.

Material and methods

OECTs fabrication

Planar OECTs were fabricated on conventional microscope glass slides (75×25 mm^2). Thermally evaporated gold defined source, drain, and gate tracks, patterned *via* lift-off lithography. PEDOT:PSS (Heraeus, Clevios PH 1000) transistor channels of 25×25 μm^2 and gate electrodes (4×4 mm^2) were created using an adapted version of the parylene C (PaC) peel-off technique.[34] Briefly, following gold lift-off an anti-adhesive layer (2% v/v industrial cleaner, Micro-90) was spin-coated (1000 rpm, 30 seconds) on the glass slide followed by deposition of a single 2 μm thick layer of parylene C (PaC). AZ9260 photoresist was then spin-coated, exposed, and developed in AZ developer (AZ Electronic Mate-

rials) followed by reactive ion etching (Oxford 80 Plasmalab plus) of the unprotected layer of PaC in order to define openings for PEDOT:PSS deposition. The conducting polymer formulation consisted of PEDOT:PSS, ethylene glycol (Sigma Aldrich, 0.25 mL for 1 mL PEDOT:PSS solution), 4-dodecylbenzenesulfonic acid (DBSA, 0.5 μL mL^{-1}) and 3-glycidoxypropyltrimethoxysilane (GOPS) (10 mg mL^{-1}). To enhance the adhesion of the PEDOT:PSS layer to the gold contacts during PaC peel-off, a monolayer of 3-mercaptopropyltrimethoxysilane (MPTMS) was formed on the gold by exposing the substrate to a 10 mM solution (3:1 volume iso-propyl alcohol (IPA)/de-ionised water (DI)) for 1 min, then rinsed with IPA and DI and blown dry with nitrogen. Prior to spin-coating of the PEDOT:PSS solution, the glass slides were O$_2$ plasma activated (25 Watt, 120 seconds) to promote hydrolysis and activation of the MPTMS.[35] The resulting devices were subsequently baked at 130 °C for 1 h followed by 2 rinsing/soaking cycles in deionized water to wash away any unbound low density molecular-weight material from the OECT channel and gate.

Microtrap design, fabrication and operation

The PDMS microfluidic trapping device was fabricated by standard soft lithography *via* SU-8 replica moulding. A silicon wafer was rinsed with acetone, IPA and DI water and then blown dry with nitrogen. The wafer was then placed in an oven at 150 °C under vacuum for at least 3 hours to dehydrate the silicon wafer and improve SU-8 adhesion. A single 250 μm thick layer of SU-8 2075 (MicroChem Corp) was spin-coated on the wafer, followed by pre-exposure baking, i-line ($\lambda = 365$ nm) exposure, post-exposure baking and development. The final master mould was then treated with an anti-adhesive layer of perfluorodecyltrichloro-silane (Nanonex nanoimprintor) to facilitate demoulding of the cured PDMS. PDMS elastomer and curing agent were mixed truly in a 10:1 weight ratio, poured on the master mould and cured at 60 °C overnight.

The PDMS microfluidic trap device comprises a single straight channel (500 μm wide) that terminates with a nozzle in order to facilitate the positioning of the spheroid at its end. Following the nozzle trap, a round chamber was designed in which the gate electrode of the transistor was located. The channel of the OECT channel was positioned on the side of the straight microfluidic channel (Fig. 1a). Loading and unloading of the spheroid from the inside of the microtrap was controlled by a gravity-driven flow by altering the liquid level in the two liquid reservoirs connected to the two extremes of the monolithic PDMS microdevice. During the spheroid trapping step the height of the liquid in one of the reservoirs of the microchannel was kept to a higher level. The recovery of the spheroid was then performed by simply inverting the liquid levels from the two liquid reservoirs. Variations in the liquid levels of the two reservoirs was carefully varied during the loading and unloading of the spheroid in order to avoid high flow rates that can impact the integrity of
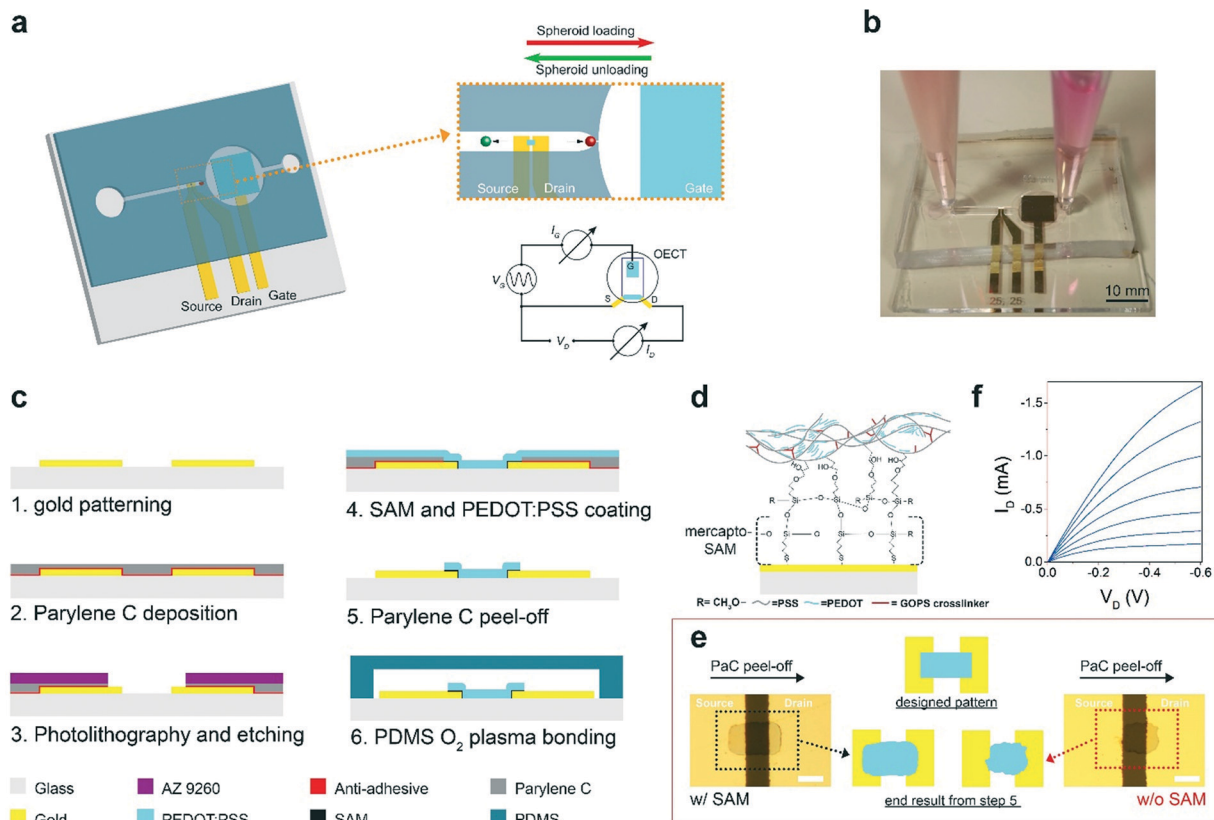
Fig. 1 (a) Schematic representation of the microtrap impedance sensing platform. An organic electrochemical transistor (OECT) is fabricated on glass and the PDMS microtrapping device is positioned on top of the planar electronics. The transistor channel ($25 \times 25 \ \mu m^2$) is located to the left of the nozzle trap while the gate is positioned right after the microtrap. Zoom in illustration shows the loading (red) and unloading (green) flow direction to place the spheroid within the microtrap. Wiring diagram of an OECT for cell impedance based sensing. (b) Optical image of the fully assembled platform in which 1 mL micropipette tips are used as permanent reservoirs for the cell culture media and to control the gravity-driven flow. (c) Modified version of standard OECT fabrication in order to achieve permanent bonding of the planar electronics and the PDMS micro-trapping device. For fabrication of the platform, (1) patterning of gold tracks, (2) deposition of anti-adhesive layer and parylene C (PaC) layer, (3) reactive ion etching for PaC patterning and gold exposition, (4) mercapto-silane self-assembled monolayer (SAM) and spincoating of PEDOT:PSS conducting polymer dispersion, (5) PaC peel-off and (6) O_2 activation for bonding. (d) Schematic illustration of the SAM-mediated covalent bonding between gold and PEDOT:PSS. The nucleophilic thiol groups selectively bond to gold, leaving the silanol moieties available to react with crosslinker in the PEDOT:PSS. (e) Enhanced adhesion between gold and PEDOT:PSS film. In the presence of the mercapto-SAM, the PEDOT:PSS film stably adheres to the gold interface after peeling off the sacrificial PaC layer. In the absence of the mercapto-SAM, we observed PEDOT:PSS tearing away from the gold layer after Pac peel off. The middle schematics show the end results of the PEDOT:PSS patterning with and without SAM after PaC peel-off. (f) Output characteristics (I_D vs. V_D) of the OECT in the presence of the SAM on gold. VG varying from 0 (top curve) to +0.6 V (bottom curve) with a step of +0.1 V.

the spheroid. Correct placement of the spheroid inside of the microtrap was verified using an inverted digital microscope. We did not make use of a bypass channel[15] to trap the spheroid as this type of microfluidic architecture is not compatible with the operation mode of cell impedance sensor. To create a circular-shaped microtrap, the un-sealed PDMS microtrap was modified as follows: (1) a glass capillary (outer diameter 80 μm) was carefully placed inside the PDMS squared microtrap (width 100 μm, height 250 μm). (2) A 125 μm thin foil of polyimide was placed on top in order to provide a reversible seal of the microtrap device. The polyimide foil was fixed in position using polyimide tape. (3) A small drop of uncured PDMS was allowed to flow by capillarity inside the microchannel in order to fill the gaps in between cured PDMS microtrap and the glass capillary. The device

was then placed in a pre-heated oven at 120 °C for 2 minutes in order to achieve a fast curing rate of the PDMS around the glass capillary. (4) The glass capillary was gently pulled out from the trap and the polyimide foil was then removed. The modified PDMS microtrap device was then fully cured for 2 hours at 80 °C. Detailed schematics of the fabrication steps are reported in Fig. S1.† Finally, inlet and outlet ports were punched in the PDMS and both microtrap and OECT device were plasma activated to obtain irreversible sealing of the microtrap device with the planar OECT.

3D spheroid cell culture

Human telomerase immortalized fibroblasts (TIF) (a gift from Ellen Van Obberghen-Schilling (Institut de Biologie de

Valrose)) and green fluorescent protein expressing canine epithelial kidney cells (MDCK II eGFP) cells (a gift from Frederic Luton (IPMC, Valbonne)) were used to prepare spheroids for both mono and co-culture. TIF pLifeAct were transfected with p^{CMV}LifeAct–TagRFP (ibidi GmbH) to achieve stable expression of red fluorescent labelling of F-actin protein. The cells were cultivated in DMEM (Advanced DMEM Reduced Serum Medium 1×, Invitrogen) with 2 mM glutamine (Glutamaxt-1, Invitrogen), 10% FBS (Fetal Bovine Serum, Invitrogen), 0.5% PenStrep (PenStrep100×, Invitrogen) and 0.1% Gentamicin (Gentamicin 100×, Invitrogen). Briefly, spheroids were growth in a 96 well hanging drop plate (InSphero, Switzerland). 40 μL cell suspensions of TIF pLifeAct and/or MDCK II eGFP were used to fill each hanging drop well. 1000 and 2000 cells per drop were used for the formation of two different sizes of TIF pLifeACT spheroids. MDCK II eGFP spheroids were cultured starting from 500 cells per drop, while TIF pLifeAct/ MDCK II eGFP co-culture spheroids were prepared using a cell ratio of 2 : 1 (1000–500 cells), respectively. This ratio was found to be optimal for enhancing self-organization of the spheroid with a characteristic core–shell structure (core: TIF pLifeAct; shell: MDCK II eGFP). Spheroid circularity was promoted using cell culture media containing 3.83 mg mL^{-1} dextran complement (Sigma-Aldrich, Switzerland), Fig. S2.†[36] Spheroids were cultured for 3 days in an incubator at 37 °C, 95% Humidity, 5% CO_2.

OECT operation and data analysis

For the operation of the OECTs, a National Instruments PXIe-1062Q system was employed. A source-measurement unit (SMU) NI PXIe-4145 was used to bias the channel of the OECT (V_{DS}), while gate potential was applied and controlled using a NI PXI-6289, a multifunction data acquisition (DAQ) module. For frequency-dependent measurements, output currents of the drain (I_D) and the gate (I_G) were recorded using two NI-PXI-4071 digital multimeters (DMM). The bandwidth measurements were performed by applying a sinusoidal modulation at the gate electrode (ΔV_{GS} = 50 mV peak-to-peak, 1 Hz < f < 20 kHz) while keeping a constant bias at the drain (V_{DS} = −0.5 V). A schematic of the wiring of an OECT is shown in Fig. 1a. Measurement parameters were controlled using a customized LabVIEW program. Fitting of the frequency-dependent measurements to extract the absolute spheroid resistance was performed using a Matlab script, as reported previously.[25] The extracted spheroid resistance values were then normalised by the area through which the ions can flow when biasing the transistor (Fig. S1.7†). The obtained spheroid resistance R_{sph} was expressed in $\Omega\ cm^2$. When using TIF and TIF/MDCK II spheroids, we estimated a cell area equal to the cross-section surface of the circular-shaped trap (diameter of 80 μm). As for MDCK II spheroids, due to insertion of the spheroid inside the circular trap, the total cell surface area was calculated by the sum of the cross-section surface of the circular-shaped trap and the lateral contact surface between spheroid and microtrap.

Results

Microtrap platform design

The OECT is a three terminal device that can be easily integrated and operated in microfluidics, as we showed previously.[32] Fig. 1a shows a schematic representation of the proposed platform, with details on the liquid flow directions for loading and unloading of the spheroid, as shown in the zoom-in schematic of Fig. 1a (red and green arrows). A picture of the fully assembled device is shown in Fig. 1b.

Fig. 1c shows a scheme of the OECT fabrication steps, including its integration with the PDMS microtrapping device, shown in step 6. Patterning of organic material, *e.g.* PEDOT: PSS, using the PaC peel-off techniques was first reported by DeFranco *et al.*[37] and successively adapted by Sessolo *et al.* for the fabrication of low impedance multi-electrode arrays for *in vitro* neural recording.[34] In our laboratory, we have successfully used the PaC peel-off technique for the fabrication of several OECT channel geometries, from millimetre scale[38] down to tens of micrometre OECT channel length.[39] For standard OECT fabrication, we make use of two separate layers of PaC (~2 μm each) to insulate the gold contacts and define the active area of the transistor by peel-off technique, respectively. PaC is one of the many derivatives of poly(*p*-xylylene) characterised by high mechanical and chemical stability. However, one of the main drawbacks in using PaC as the insulator layer for planar OECT is its chemical incompatibility with PDMS. In practice, PDMS and PaC cannot be bonded permanently together by simple O_2 plasma activation, a common technique used to seal PDMS microfluidics onto glass substrates. To overcome this limitation, we modified the OECT fabrication protocol using only a single layer of PaC. By doing so, we are able to pattern the PEDOT: PSS film to form an OECT and, at the same time, to use the glass substrate for bonding *via* O_2 activation of the PDMS microtrapping device with our planar electronics.

In the new fabrication protocol, following lift-off to define gold tracks (step 1 Fig. 1c), a single 2 μm thick layer of PaC was deposited (step 2). Patterning of the transistor active areas, both OECT channel and gate electrode, was achieved by O_2 reactive-ion etching (RIE), step 3. To promote a stable covalent bonding between the gold and the conducting polymer film, a self-assembled monolayer (SAM) of the (3-mercaptopropyltrimethoxy)-silane was formed on the gold contacts. Covalent crosslinking between the mercapto-SAM and the spin-coated PEDOT: PSS film is possible due to the presence of a second silane agent (GOPS) dispersed in the PEDOT: PSS liquid suspension. A schematic of the chemical structures of the mercapto-SAM and its crosslinking network within the PEDOT: PSS film is shown in Fig. 1d. The impact of the mercapto-SAM on the electrochemical behaviour of the OECT active layer was assessed by cyclic voltammetry and impedance spectroscopy, both confirming negligible effects (more details shown in ESI,† Fig. S3). Finally, the PaC layer was peeled-off to reveal the final pattern of the conducting polymer film, as shown in Fig. 1c step 5.

It is important to note that initial attempts to fabricate fully operative and stable OECT devices without the use of the mercapto-SAM were unsuccessful. The mechanical stress generated at the PEDOT : PSS film/gold interface during mechanical removal of the single PaC layer resulted in delamination of the conducting polymer film and, in turn, failure in the transistor operation. Improvements in the OECT fabrication due the presence of the mercapto-SAM are presented in Fig. 1e. Fig. 1f shows the transfer characteristics of an OECT as a function of the gate bias, following mercapto-SAM functionalization. The drain current (I_D)/voltage drain (V_D) characteristic demonstrates a typical low voltage operation (below 1 V) in depletion mode.[26]

Fig. 2a shows time-lapse images of the spheroid trapping steps. As the spheroid can be easily trapped using our microtrap architecture, the next step was to achieve optimal performance of the impedance sensor when embedded in the microfluidics. One the main challenges to face when measuring the impedance of 3D spheroids is to drive the ion flux through the spheroid and to avoid any other low resistive ionic pathways, as they can lead to misinterpretation of the device readout. Standard photolithographic fabrication of master moulds for PDMS replica moulding makes use of a single layer of the negative SU-8 photoresist. However, when using SU-8 master moulds the resulting PDMS microfluidic chips can only be made with a squared cross-section profile due to the impossibility to reflow the photoresist after development. Fig. 2b-i and ii show optical images of the PDMS microdevice and a schematic view of the cross section of the nozzle microtrap, respectively. Although this trap geometry has been shown by others to be effective for spheroid trapping,[14,15,18] the use of the squared profile microtrap leads to the presence of gaps in between the PDMS and the spheroid, highlighted by the black arrows in the scheme of Fig. 2b-iii.
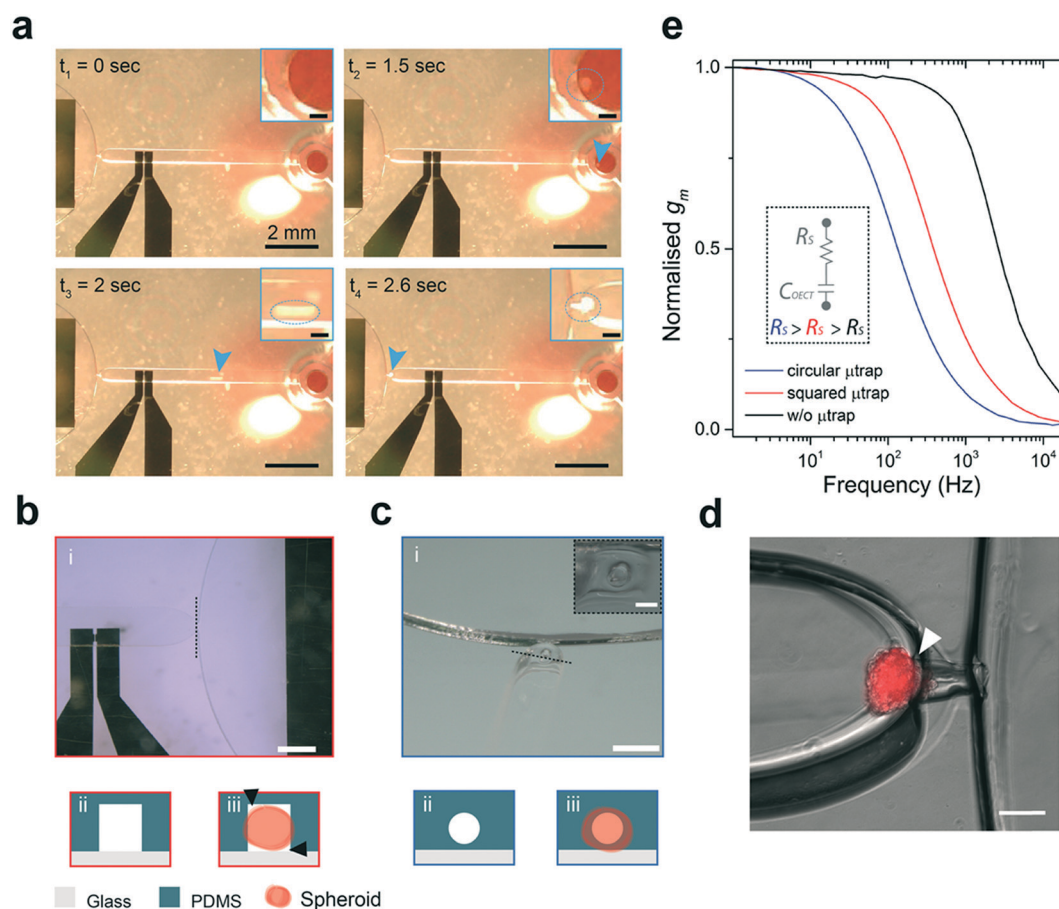
Fig. 2 (a) Time lapse images of the spheroid trapping. From top left to bottom right, (t_1) placing the spheroid in the inlet reservoir, (t_2) spheroid reaching the PDMS inlet, (t_3) spheroid travelling through the microchannel and (t_4) spheroid trapped in the microfluidic nozzle. (b) top – Optical image of the microtrap for the fully assembled platform (scale bar 500 μm). bottom –Schematics of the cross-sectional view of the squared microtrap and spheroid trapping. The squared profile can lead to the presence of gaps between the spheroid and the PDMS (black arrows). (c) top – Optical image of the modified version of the microtrap using the glass capillary templating technique. Inset image showing a close up view of the circular-shaped microtrap (scale bar 500 μm, inset 100 μm). bottom – Schematics of the cross-sectional view of the circular-shaped microtrap and spheroid trapping. (d) Optical image of a TIF pLifeAct spheroid trapped in the circular-shaped trap. The white arrow shows the conformal contact between the spheroid and the PDMS (scale bar 100 μm). (e) Frequency dependent response of the OECT in microfluidics in the absence of the microtrap (black), when using the squared microtrap (red) and the circular-shaped microtrap (blue). The decrease in the cut-off frequency (−3 dB) is due to the increase of the series resistance in the electrolyte.

This in turn can cause loss in sensitivity of the impedance sensor as the ionic current can flow through those gaps as they hold a lower ionic resistance compared to the paracellular ones. In support of this, Huerta *et al.* showed already the impossibility to measure impedance of cysts with a diameter smaller than the inner diameter (ID) of the glass micro capillary (Ø = 164 μm) used for the trapping.[33] As the envisioned platform should be able to reliably measure the impedance for spheroids of different radii, we modified the squared microtrap profile to achieve a circular-shaped nozzle profile that can be easily used with spheroids of different dimensions. An optical image of the PDMS modified microtrap and a close up picture of the circular-shaped profile (inset) is shown in Fig. 2c-i. Details on the post-modification of the microtrap using the glass capillary templating technique can be found in Fig. S1.† Schematics of the cross-sectional view of the circular-shaped profile of the trap and envisioned trapping of the spheroid are shown in Fig. 2c. The use of this microtrap geometry can provide a better seal of the spheroid around the microtrap perimeter and greatly favour the operation of the impedance sensor by minimising the ionic flow around the spheroid. Moreover, another advantage of using the circular-shaped trap is the possibility to trap and measure impedance of any spheroid as long as their diameter is larger than 80 μm, *i.e.* circular trap diameter. Fig. 2d shows a TIF-pLifeAct spheroid of a diameter equal to ~149 μm trapped in the circular-shaped nozzle where a tight contact between the spheroid and the PDMS is clearly visible, as indicated by the white arrow.

Alongside the improvements of the trapping microstructure, it was also important to assess the impact of the microtrap on the performance of the OECT in its operational frequency range (1 Hz $\leq f \leq$ 20 kHz). In fact, by placing the nozzle in between the gate and the channel of the transistor a change in the transistor response is expected due to an increased electrolyte ionic resistance (R_{el}). Fig. 2e shows a direct comparison of the bandwidth spectra (transconductance g_m *vs.* frequency) for the OECT in the absence and presence of the microtrap. The transconductance g_m represents the gain (amplification) of the transistor ($\Delta I_D/\Delta V_G$). Fig. 2e shows the frequency dependent characteristic of the OECT when both the transistor gate and channel were placed in the straight microfluidic channel, right before the nozzle microtrap. A characteristic plateau of g_m is observed up to ~700 Hz, followed by an abrupt decrease in the transconductance at higher frequencies and a resulting cut-off frequency (−3 dB) at ~1.47 kHz. The inset image of Fig. 2e shows an equivalent circuit for which the capacitor is the OECT capacitance (C_{OECT}) and R_s is the series resistance, including the electrolyte resistance R_{el}. In the presence of the squared and circular-shaped microtrap, a slightly different g_m *vs.* frequency characteristic was measured, with a shift of the cut-off frequency towards lower frequencies due to the increase in the R_{el} contribution in both cases. We measured a cut-off frequency of ~190 Hz (red) for the squared and unmodified microtrap, and ~63 Hz (blue) when using the circular-shaped

microtrap. For the latter, the lower cut-off frequency is consistent with the fact that the circular-shaped microtrap has a smaller cross-sectional area (higher R_{el}) compared to the squared one, as shown in the inset equivalent circuit of Fig. 2e.

Microtrap platform performance

The main objective of this work was to realise a platform capable of measuring the electrical resistance of spheroids (R_{sph}) in a simple and reliable manner. To validate our platform, we first made use of fluorescently labelled TIF (pLifeAct expressing RFP actin) spheroids. Spheroids were cultured using two different conditions in order to achieve spheroids of different dimensions. Using a static hanging drop plate, we were able to grow these spheroids with an average diameter of 152 ± 4 μm and 187 ± 11 μm by seeding 1000 and 2000 cells per drop, respectively. Fig. 3a shows the typical bandwidth spectra for the transistor when a single TIF pLifeAct spheroid was placed inside the microtrap. When using the OECT to measure the spheroid impedance, a further decrease in the initial cut-off frequency of the transistor was monitored due to changes in the ion flux caused by the presence of the spheroid in the microtrap, from the blue curve to the orange and green curves. Fig. 3b shows optical images for the two spheroids with a diameter of ~140 μm for the 1000 cells and a diameter of ~184 μm for the 2000 cells when trapped in the circular-shaped nozzle. The two insets of Fig. 3b show the fluorescence images of the spheroids prior to trapping, showing almost unaltered shape of the spheroids once inside the microtrap. We can also observe how the two spheroids present a good contact to the circular-shaped trap despite their different diameters.

With regards to the transistor cut-off frequency change given by the two TIF spheroids, we observed in this case only a slight difference in the final cut-off frequencies, *i.e.* ~2 Hz. Fig. 3c shows the extracted impedance spectra measured in the absence of spheroids (blue curve), and when the two spheroids were placed in the microtrap (1000 cells, green curve; 2000 cells, orange curve). The inset equivalent circuit of Fig. 3c was used to fit the impedance spectra in order to extract the spheroid resistance values R_{sph} for the two TIF spheroids. It should be noted here that R_{sph} takes into account the ionic resistive pathways both through and around the spheroid. Although the circular-shaped trap is able to significantly improve the seal between the PDMS microtrap and the spheroid, the presence of gaps contributing to the final impedance cannot be excluded. The estimated R_{sph} for the ~140 μm spheroid is 3.6 Ω cm² and for the ~184 μm spheroid the R_{sph} is equal to 4.1 Ω cm². The slightly larger R_{sph} of the latter spheroid might be attributed to its larger dimension as this spheroid can impede more the ion flow when compared to the smaller one. However, when comparing the mean R_{sph} values for several spheroids in Fig. 3d (1000 cells R_{sph} = 3.9 Ω cm² (n = 4), 2000 cells R_{sph} = 4.4 Ω cm² (n = 4)), there is not a statistically significant difference (p < 0.05,
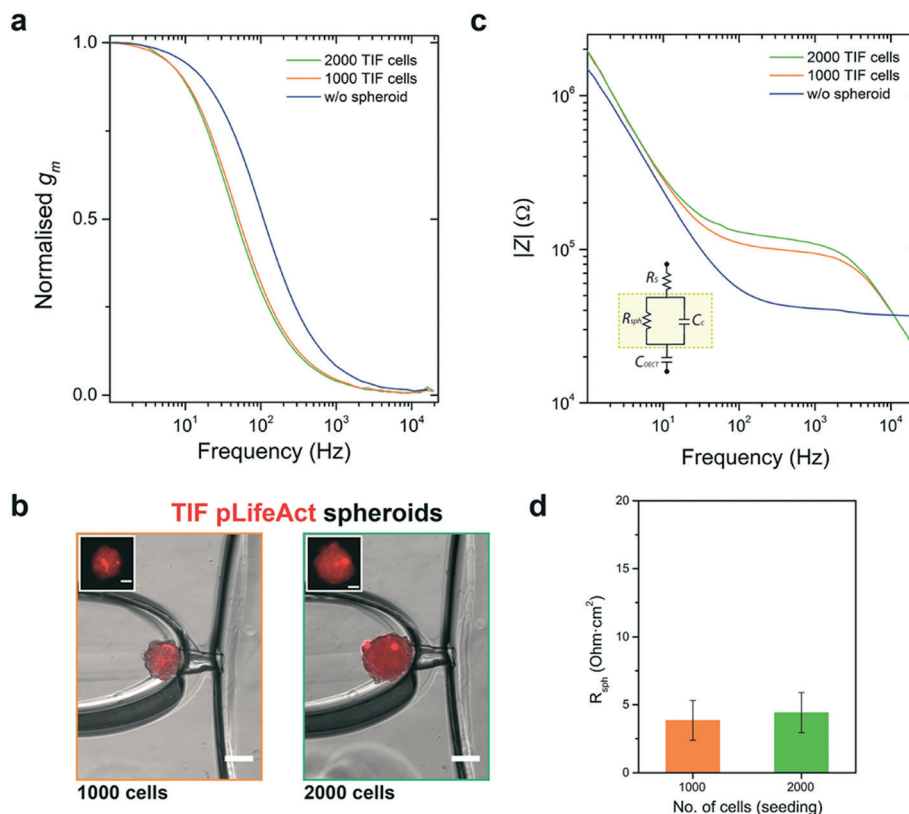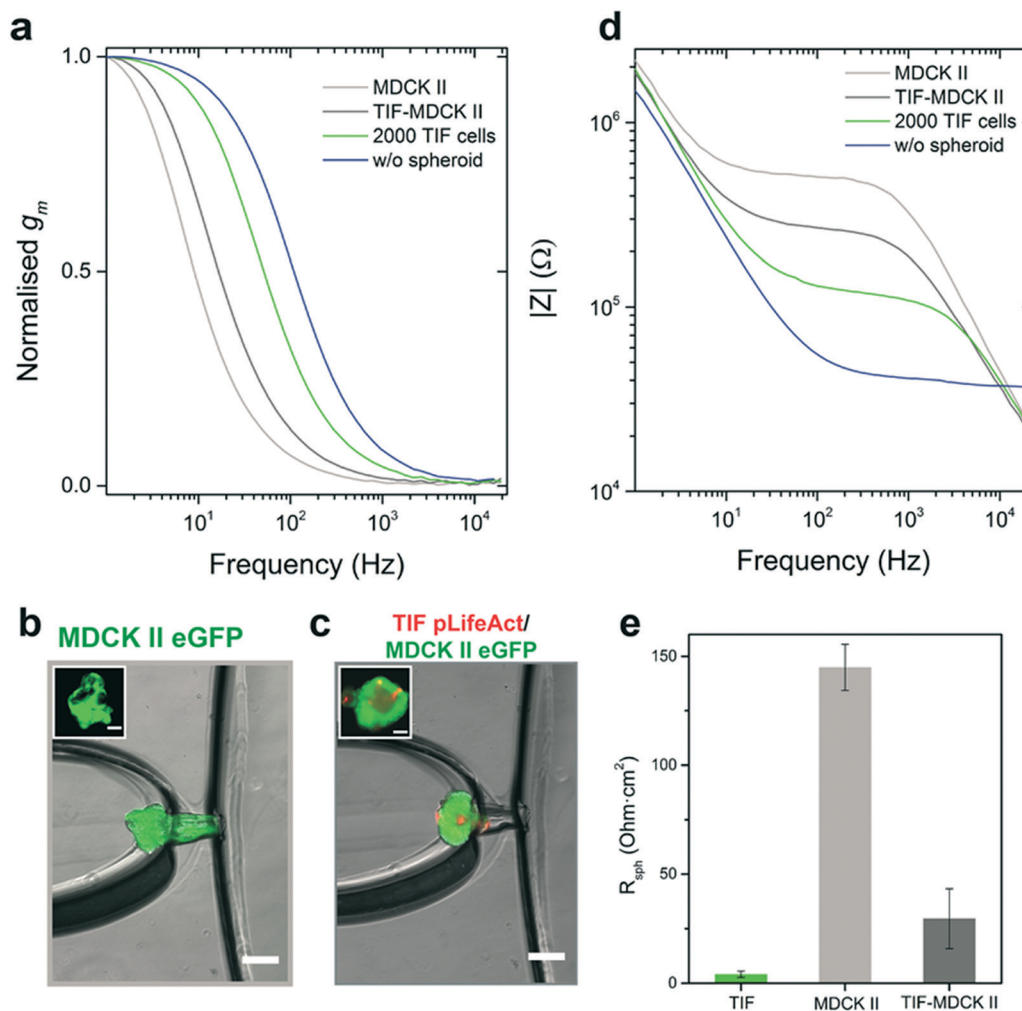
Fig. 3 (a) Typical frequency dependent response of the OECT in the absence (blue) and in the presence of TIF pLifeACT spheroids of different dimensions. Seeding conditions for the spheroid: 1000 cells per drop (orange) and 2000 cells per drop (green). (b) left – 1000 cells spheroid (Ø = ca. 140 μm) trapped inside the circular-shaped nozzle. Inset image shows the spheroid prior trapping (scale bar 100 μm, inset 50 μm). right – 2000 cells spheroid (Ø = ca. 184 μm) trapped inside the circular-shaped nozzle. Inset image shows the spheroid prior to trapping (scale bar 100 μm, inset 50 μm). (c) Typical impedance spectra in the absence (blue) and presence of TIF pLifeAct spheroids (1000 cells, orange; 2000 cells, green). Inset equivalent circuit used for the fitting of the spheroid resistance (R_{sph}). (d) R_{sph} obtained for different TIF pLifeAct spheroids cultured using the two conditions. (1000 cells $n = 4$, 2000 cells $n = 4$).

t-test). TIF cells' primary role is structural, being largely present in connective tissue rather than epithelial or endothelial (barrier-tissue). Therefore, this result showed us the R_{sph} is largely dependent on the ion permeability of the spheroid, i.e. cell type and function, rather than its dimensions.

Following this result, we then wanted to investigate the ability of the platform to measure the R_{sph} when different cell types are used for the formation of the spheroids. MDCK II cells are epithelial cells from the distal part of the kidney tubule that express TJs in their apical cellular membrane and are highly resistive when cultured in 2D.[32] Initial attempts to grow MDCK II spheroids using the hanging drop technique were not successful as we could only form cellular clusters with dimensions well below the circular-shaped trap diameter, i.e. 80 μm. Yonemura et al.[9] observed a similar behaviour when growing MDCK II cells in U-bottomed culture plates. As a means to improve spheroid formation, we made use of dextran (see Materials and methods) added to the cell culture media in order to increase the media viscosity and favour spheroid formation. By doing so, we were able to form much larger MDCK II organoids, although we could not achieve high yield. An optical image of the trapped MDCK II eGFP organoid is presented in Fig. 4b. The inset of Fig. 4b shows

the organoid prior to trapping in the circular-shaped nozzle. In this case, we noticed that the MDCK II eGFP organoids had a much softer nature compared to the TIF spheroids as the trapping always resulted in the spheroid being drawn into the length of the circular trap. Changes in the relative height of the liquid in the inlet/outlet reservoirs to achieve lower flow rates were not sufficient to avoid the confinement of the organoid throughout the trap. The softer nature of the MDCK II eGFP cluster may be due to the formation of a lumen, resulting in formation of a cyst rather than a spheroid, previously described under the culturing conditions used here.[9] When measuring the impedance of the R_{sph} for the MDCK II-eGFP cyst, we observed a drastic decrease in the transistor cut-off frequency (below 5 Hz) as shown by the light grey curve in Fig. 4a. Resulting impedance spectra and mean R_{sph} values of $145 \pm 11 \ \Omega \ cm^2$ ($n = 2$) for the MDCK II-eGFP cyst are shown in Fig. 4d and e, respectively. With regards to the much higher R_{sph}, we believe this may be caused by the typical lower ion permeability of this type of cells as well as the much tighter contact between the cells due to the cyst deformation/compression inside the circular-shaped nozzle. This result demonstrates that the platform can easily detect difference in the spheroid ion permeability; however, we needed

Fig. 4 (a) Typical frequency dependent response of the OECT in the absence (blue) and in the presence of TIF pLifeACT spheroid (green), TIF pLifeAct/MDCK II eGFP co-cultured spheroid (grey) and MDCK II eGFP spheroid (light grey). (b) MDCK II eGFP spheroid (Ø = ca. 145 μm) trapped inside the circular-shaped nozzle. Due to the presence of a cyst lumen, the cyst presents a soft nature that results in the insertion of the spheroid inside the circular-shaped trap. Inset image shows the spheroid prior trapping (scale bar 100 μm, inset 50 μm). (c) TIF pLifeAct/MDCK II eGFP co-cultured spheroid (Ø = ca. 183 μm) trapped inside the circular-shaped nozzle. Inset image shows the spheroid prior trapping (scale bar 100 μm, insert 50 μm). (d) Typical impedance spectra in the absence (blue) and in the presence of TIF pLifeACT spheroid (green), TIF pLifeAct/MDCK II eGFP co-cultured spheroid (grey) and MDCK II eGFP spheroid (light grey). (e) Mean R_{sph} obtained for different spheroid types: TIF pLifeAct (2000 cells n = 4), MDCK II eGFP (n = 2) and TIF pLifeAct/MDCK II eGFP (n = 5).

further evidence of this due to the unexpected insertion of the MDCK II eGFP cyst inside the microtrap.

We had shown before that TIF pLifeAct spheroids were not deformed (Fig. 3) when trapped in the platform. Given their supporting tissue function, we wanted to use them in combination with MDCK II cells for the formation of a more mechanically stable spheroid. In this case, the TIF cells should provide a suitable matrix on which the MDCK II can grow and form a continuous cell barrier. Interestingly, the co-culture of the two cell types resulted in the formation of spheroids with a core–shell structure in which the core is made of TIF cells while the MDCK II cells form a confluent layer around the core. The insert image of Fig. 4b shows a typical TIF/MDCK II spheroid where it is possible to observe a more dense core of TIF cells (red) surrounded by the MDCK

II (green) epithelial cells. Fig. 4b shows a trapped TIF/MDCK II spheroid that did not deform after trapping, similar to what we observed previously when only using TIF cells for the spheroid. When measuring the R_{sph} for the TIF/MDCK II spheroid, we obtained typical resistance values higher than the TIF spheroid but lower than the MDCK II ones. Co-cultured spheroids were characterised by a cut-off frequency of ~10 Hz, as shown in Fig. 4a. Fig. 4e reports values of R_{sph} equal to 29.3 ± 13.7 Ω cm² (n = 5) for an average spheroid dimension of 206 ± 66 μm. In the same graph resistance value of TIF spheroids (2000 cells) are also reported, for a more straightforward graphical comparison of the differences in R_{sph} of the three spheroid types. Overall, these results provide clear evidence of how the measured R_{sph} is influenced by the differences in the spheroid ion permeability given by the cells
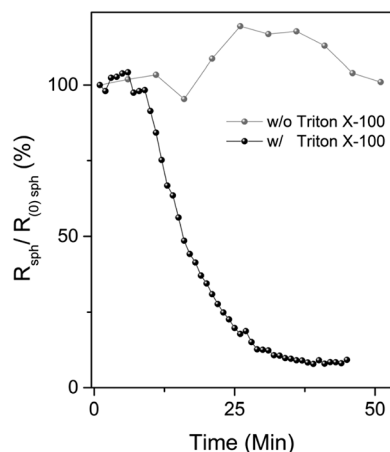
Fig. 5 On line measurements of the R_{sph} in the presence (black/white dots) and absence (grey/white dots) of a porogenic agent, triton X-100, 170 μM. Due to the presence of triton X-100 in cell culture media, a continuous decrease in R_{sph} was measured resulting from the gradual disruption of the spheroid cells membrane integrity.

and, that the combination of the OECT with the circular-shaped microtrap is a suitable platform to assess such differences.

To further validate the platform, we also tested the dynamic performance of the device. Fig. 5 shows dynamic measurements over a period of 45 minutes during which the TIF/MDCK II spheroid is exposed to a porogenic molecule, Triton X-100, a well-known non-ionic surfactant. The positive control experiment shows that the transistor performance was not affected by the presence of the Triton X-100 in the electrolyte (Fig. S6†). The variation of the R_{sph} (circle black) for a co-culture of TIF/MDCK II spheroid exposed to a concentration equal to 170 μM of Triton X-100 shows that it takes *ca.* 10 minutes to observe an initial decrease in the R_{sph}. Following this time, a more marked variation of the R_{sph} was then recorded with a total loss of ~90% of the initial resistance after *ca.* 35 minutes of exposure to Triton X-100. The control experiment in the absence of Triton X-100 in Fig. 5 (grey circle) does not show a similar trend and the R_{sph} is stable over the same period of time. However, some variations in the R_{sph} were measured probably due to movements of the spheroid within the trap during the testing period.

General discussion

In this work we have developed a novel platform to perform impedance sensing of 3D spheroids. The platform comprises a circular-shaped PDMS microfluidic trapping device and an OECT impedance sensor to measure the R_{sph}.

The proposed platform is capable of measuring the impedance of different kinds of spheroids. When using TIF spheroids we obtained R_{sph} values of just a few $\Omega\ cm^2$. The low resistance seems to be in agreement with the fact that fibroblast cells have a supporting tissue function and do not

present significant paracellular resistance. When varying the spheroid diameter we observed negligible differences in the R_{sph} of TIF spheroids, understood as a change in the ionic pathways when flowing through a larger or smaller spheroid. We showed the suitability of this platform for measuring R_{sph} for spheroids that present different ionic permeability as they were grown using different cell types. For TIF/MDCK II spheroids we obtained average R_{sph} values ~6.7 times larger than for TIF pLifeAct. Although these two spheroids types present comparable dimensions (TIF/MDCK II spheroid diameter equal to 206 ± 66 μm and TIF pLifeAct spheroids (2000 cells) average diameter equal to 187 ± 11 μm) a marked difference in the R_{sph} was measured due to the presence of highly resistive MDCK II epithelial cells on the spheroid outer shell.

When looking at other 3D spheroid impedance platforms, *e.g.* making use of microcavities,[22] hanging drop systems,[23,24] capillary traps[40] and others,[41] one of their current limitations is the absence of a common physical quantity to describe the spheroid impedance. Different parameters/units had been used when studying the spheroid impedance, for example by comparing changes of the impedance magnitude at multiple frequencies,[24] normalised current[23] and relative increase of the full impedance frequency spectrum.[22,40,41] Although these methods are suitable to describe the 3D *in vitro* models under investigation, it is difficult to have a straightforward comparison between the outcomes of these studies. For impedance sensors in 2D cell cultures, TEER is the gold-standard parameter employed by most of the commercially available impedance systems, such as cellZscope, chopstick electrodes and ECIS from Applied BioPhysics. However, the TEER describes the trans(endo/epi)thelial resistance of a single cell monolayer while in spheroids the cells are clustered together in a 3D configuration. Thus, TEER is not a suitable parameter to be used when studying the impedance of 3D spheroids. As an alternative, in this work we made use of the R_{sph} as the physical quantity of interest to describe the impedance of spheroids expressed in $\Omega\ cm^2$ units. Indeed, we were able to show a correlation between spheroid resistance R_{sph} and differences in the spheroid ionic permeability arising from the use of different cell, as well as online assessment of the R_{sph} in the presence of a porogenic agent. To conclude, it should be stressed here once more that R_{sph} should solely describe the ionic paracellular resistance in 3D, however, we cannot exclude the presence of ionic pathways around the spheroids. Our strategy here was to use the circular-shaped nozzle to improve the seal contact between spheroid and PDMS trap and minimise/avoid the presence of gaps that can lead to potential low resistive ion fluxes around the spheroid. Further studies on this aspect are currently underway.

Conclusions

In this work, we have proposed a novel platform combining a circular-shaped microtrap and OECTs to accurately measure the impedance of 3D spheroids. A new photolithographic fabrication protocol was developed for the fabrication of the

OECTs through the use of a mercapto-silane agent to improve the adhesion between PEDOT : PSS/gold and we showed standard OECT performance. Moreover, the new fabrication protocol favoured the integration of PDMS based microfluidics, otherwise impossible when using the 2-layers PaC fabrication due to the chemical incompatibility for bonding between PaC and PDMS.[34] The spheroid microfluidic trap consisted of a single channel terminating with a nozzle trap geometry. To improve the spheroid ionic blockage between the channel and the gate of the OECT, the nozzle trap was modified to achieve a circular-shaped profile that minimises/avoids the presence of gaps between spheroid and PDMS trap contours. The modified trap was used to measure the impedance of spheroids in a non-destructive way. When using the platform to measure the impedance of 3D spheroids, we showed marked differences in the R_{sph} for spheroids grown using fibroblast and epithelial cells alone, and when combining the two cell types. Finally, we assessed the platform performance while measuring in real-time changes in the R_{sph} caused by the presence of a triton X-100 in the cell media, known to disrupt cell membrane integrity.

Future work will focus on making improvements to the spheroid trapping mechanism to avoid unwanted insertion of the spheroid inside the circular-shaped trap when using softer spheroids and/or cysts, such as the MDCK II organoids here. This can possibly be achieved by microfabrication of a smaller circular-shaped microtrap using laser ablation.[42] Further improvements on the estimation of R_{sph} will be also addressed in the future by correlating the spheroid impedance with its volume instead of the contact surface area between spheroid and microtrap.

Conflicts of interest

There are no conflicts to declare.

Acknowledgements

Notes and references

1 E. R. Shamir and A. J. Ewald, *Nat. Rev. Mol. Cell Biol.*, 2014, **15**, 647–664.
2 N. T. Elliott and F. Yuan, *J. Pharm. Sci.*, 2011, **100**, 59–74.
3 E. Carletti, A. Motta and C. Migliaresi, in *3D Cell Culture: Methods and Protocols*, ed. J. W. Haycock, Humana Press, Totowa, NJ, 2011, pp. 17–39.
4 T.-M. Achilli, J. Meyer and J. R. Morgan, *Expert Opin. Biol. Ther.*, 2012, **12**, 1347–1360.
5 F. Oltolina, A. Zamperone, D. Colangelo, L. Gregoletto, S. Reano, S. Pietronave, S. Merlin, M. Talmon, E. Novelli, M. Diena, C. Nicoletti, A. Musarò, N. Filigheddu, A. Follenzi and M. Prat, *PLoS One*, 2015, **10**(9), e0137999.
6 L. Polonchuk, M. Chabria, L. Badi, J.-C. Hoflack, G. Figtree, M. J. Davies and C. Gentile, *Sci. Rep.*, 2017, **7**, 7005.
7 S.-A. Lee, D. Y. No, E. Kang, J. Ju, D.-S. Kim and S.-H. Lee, *Lab Chip*, 2013, **13**, 3529–3537.
8 C. C. Bell, D. F. G. Hendriks, S. M. L. Moro, E. Ellis, J. Walsh, A. Renblom, L. F. Puigvert, A. C. A. Dankers, F. Jacobs, J. Snoeys, R. L. Sison-Young, R. E. Jenkins, Å. Nordling, S. Mkrtchian, B. K. Park, N. R. Kitteringham, C. E. P. Goldring, V. M. Lauschke and M. Ingelman-Sundberg, *Sci. Rep.*, 2016, **6**, srep25187.
9 S. Yonemura, *PLoS One*, 2014, **9**, e112922.
10 K. Ray, *Nat. Rev. Gastroenterol. Hepatol.*, 2014, **11**, 516–516.
11 Y.-C. Tung, A. Y. Hsiao, S. G. Allen, Y. Torisawa, M. Ho and S. Takayama, *Analyst*, 2011, **136**, 473–478.
12 L. Li, Q. Zhou, T. C. Voss, K. L. Quick and D. V. LaBarbera, *Methods*, 2016, **96**, 97–102.
13 J. Friedrich, C. Seidel, R. Ebner and L. A. Kunz-Schughart, *Nat. Protoc.*, 2009, **4**, 309–324.
14 K. S. McMillan, M. Boyd and M. Zagnoni, *Lab Chip*, 2016, **16**, 3548–3557.
15 P. N. Silva, B. J. Green, S. M. Altamentova and J. V. Rocheleau, *Lab Chip*, 2013, **13**, 4374.
16 K. Kwapiszewska, A. Michalczuk, M. Rybka, R. Kwapiszewski and Z. Brzózka, *Lab Chip*, 2014, **14**, 2096–2104.
17 W. Liu, J.-C. Wang and J. Wang, *Lab Chip*, 2015, **15**, 1195–1204.
18 J. Ruppen, L. Cortes-Dericks, E. Marconi, G. Karoubi, R. A. Schmid, R. Peng, T. M. Marti and O. T. Guenat, *Lab Chip*, 2014, **14**, 1198–1205.
19 O. Frey, P. M. Misun, D. A. Fluri, J. G. Hengstler and A. Hierlemann, *Nat. Commun.*, 2014, **5**, 4250.
20 C. M. Lo, C. R. Keese and I. Giaever, *Biophys. J.*, 1995, **69**, 2800–2807.
21 B. Srinivasan, A. R. Kolli, M. B. Esch, H. E. Abaci, M. L. Shuler and J. J. Hickman, *J. Lab. Autom.*, 2015, **20**, 107–126.
22 D. Kloß, M. Fischer, A. Rothermel, J. C. Simon and A. A. Robitzki, *Lab Chip*, 2008, **8**, 879–884.
23 S. Rismani Yazdi, A. Shadmani, S. C. Bürgel, P. M. Misun, A. Hierlemann and O. Frey, *Lab Chip*, 2015, **15**, 4138–4147.
24 Y. R. F. Schmid, S. C. Bürgel, P. M. Misun, A. Hierlemann and O. Frey, *ACS Sens.*, 2016, **1**, 1028–1035.
25 J. Rivnay, M. Ramuz, P. Leleux, A. Hama, M. Huerta and R. M. Owens, *Appl. Phys. Lett.*, 2015, **106**, 043301.
26 D. Khodagholy, J. Rivnay, M. Sessolo, M. Gurfinkel, P. Leleux, L. H. Jimison, E. Stavrinidou, T. Herve, S. Sanaur, R. M. Owens and G. G. Malliaras, *Nat. Commun.*, 2013, **4**, 2133.
27 A.-M. Pappa, V. F. Curto, M. Braendlein, X. Strakosas, M. J. Donahue, M. Fiocchi, G. G. Malliaras and R. M. Owens, *Adv. Healthcare Mater.*, 2016, **3**, 17028.
28 I. Gualandi, D. Tonelli, F. Mariani, E. Scavetta, M. Marzocchi and B. Fraboni, *Sci. Rep.*, 2016, **6**, 35419.
29 D. Khodagholy, T. Doublet, P. Quilichini, M. Gurfinkel, P. Leleux, A. Ghestem, E. Ismailova, T. Hervé, S. Sanaur, C. Bernard and G. G. Malliaras, *Nat. Commun.*, 2013, **4**, 1575.

30 C. Yao, Q. Li, J. Guo, F. Yan and I.-M. Hsing, *Adv. Healthcare Mater.*, 2015, **4**, 528–533.

31 L. H. Jimison, S. A. Tria, D. Khodagholy, M. Gurfinkel, E. Lanzarini, A. Hama, G. G. Malliaras and R. M. Owens, *Adv. Mater.*, 2012, **24**, 5919–5923.

32 V. F. Curto, B. Marchiori, A. Hama, A.-M. Pappa, M. P. Ferro, M. Braendlein, J. Rivnay, M. Fiocchi, G. G. Malliaras, M. Ramuz and R. M. Owens, *Microsyst. Nanoeng.*, 2017, **3**, 17028.

33 M. Huerta, J. Rivnay, M. Ramuz, A. Hama and R. M. Owens, *APL Mater.*, 2015, **3**, 030701.

34 M. Sessolo, D. Khodagholy, J. Rivnay, F. Maddalena, M. Gleyzes, E. Steidl, B. Buisson and G. G. Malliaras, *Adv. Mater.*, 2013, **25**, 2135–2139.

35 W. Wu, J. Wu, J.-H. Kim and N. Y. Lee, *Lab Chip*, 2015, **15**, 2819–2825.

36 B. M. Leung, S. C. Lesher-Perez, T. Matsuoka, C. Moraes and S. Takayama, *Biomater. Sci.*, 2015, **3**, 336–344.

37 J. A. DeFranco, B. S. Schmidt, M. Lipson and G. G. Malliaras, *Org. Electron.*, 2006, **7**, 22–28.

38 M. Ramuz, A. Hama, M. Huerta, J. Rivnay, P. Leleux and R. M. Owens, *Adv. Mater.*, 2014, **26**, 7083–7090.

39 A.-M. Pappa, V. F. Curto, M. Braendlein, X. Strakosas, M. J. Donahue, M. Fiocchi, G. G. Malliaras and R. M. Owens, *Adv. Healthcare Mater.*, 2016, **5**, 2295–2302.

40 C. Hildebrandt, H. Büth, S. Cho, Impidjati and H. Thielecke, *J. Biotechnol.*, 2010, **148**, 83–90.

41 K. Luongo, A. Holton, A. Kaushik, P. Spence, B. Ng, R. Deschenes, S. Sundaram and S. Bhansali, *Biomicrofluidics*, 2013, **7**, 034108.

42 Y.-K. Hsieh, S.-C. Chen, W.-L. Huang, K.-P. Hsu, A. K. Gorday, T. Wang and J. Wang, *Polymer*, 2017, **9**(7), 242.